PAPER

Edge loss of high-harmonic fast-wave heating power in NSTX: a cylindrical model

IOP Publishing | International Atomic Energy Agency Nuclear Fusion

Nucl. Fusion **57** (2017) 116062 (13pp) https://doi.org/10.1088/1741-4326/aa7860

Edge loss of high-harmonic fast-wave heating power in NSTX: a cylindrical model

R.J. Perkins, J.C. Hosea, N. Bertelli, G. Taylor and J.R. Wilson

Princeton Plasma Physics Laboratory, Princeton, NJ 08540, United States of America

E-mail: rperkins@pppl.gov

Received 26 January 2017, revised 3 May 2017
Accepted for publication 9 June 2017
Published 4 September 2017

Abstract

Efficient high-harmonic fast-wave (HHFW) heating in the National Spherical Torus Experiment Upgrade (NSTX-U) would facilitate experiments in turbulence, transport, fast-ion studies, and more. However, previous HHFW operation in NSTX exhibited a large loss of fast-wave power to the divertor along the scrape-off layer field lines for edge densities above the fast-wave cutoff. It was postulated that the wave amplitude is enhanced in the scrape-off layer due to cavity-like modes, and that these enhanced fields drive sheath losses through RF rectification. As part of ongoing work to confirm this hypothesis, we have developed a cylindrical cold-plasma model to identify and understand scenarios where a substantial fraction of wave power is confined to the plasma periphery. We previously identified a peculiar class of modes, named annulus resonances, that conduct approximately half of their wave power in the periphery and can also account for a significant fraction of the total wave power. Here, we study the influence of annulus resonances on wave field reconstructions and find instances where annulus-resonant modes dominate the spectrum and trap over half of the total wave power at the edge. The work is part of an ongoing effort to determine the mechanism underlying these scrape-off layer losses in NSTX, identify optimal conditions for operation in NSTX-U, and predict whether similar losses occur for the ion-cyclotron minority heating scheme for both current experiments and future devices such as ITER.

Keywords: ICRF, heating, tokamaks, edge loss

(Some figures may appear in colour only in the online journal)

1. Introduction

High-harmonic fast-wave (HHFW) heating is a promising heating scheme for the National Spherical Torus Experiment Upgrade (NSTX-U). HHFW heating complements neutral beam injection by heating discharges without particle or momentum input and would enable experiments in transport [1], low-rotation scenarios, and fast-particle modes [2]. Furthermore, as the plasma-facing tiles of NSTX-U transition from graphite to high- Z metal walls in the coming years, HHFW heating may play a crucial role in impurity expulsion via central RF heating, as demonstrated in conventional tokamaks [3, 4].

Unfortunately, efficient fast-wave heating is difficult to achieve in certain NSTX scenarios. Poor heating efficiency has been observed for lower antenna phasing and lower toroidal fields [5, 6] but improves with the lower scrape-off layer (SOL) density provided by lithium wall conditioning, provided that the machine is not vented to produce lithium compounds [7]. The lower heating efficiency is likely caused by a direct loss of wave power to the SOL, as evidenced by the bright spirals that formed in the upper and lower divertors [8] along field lines passing in front of the antenna [9]. The heat flux under the spirals is about 2 MW m^{-2} for an applied HHFW power of 1.8 MW. The losses are now thought to be caused by significant fast-wave propagation in the SOL when the right-hand cutoff layer, defined by $n_{\|}^2 = R$ with $n_{\|}$ denoting the parallel refractive index and R the cold-plasma dielectric component from Stix notation [10], is positioned close to the antenna [6]. Subsequent conversion of the wave power to a heat flux is believed to be caused by RF rectification [11]. Full-wave simulations of NSTX using the full-wave code AORSA [12] with the solution domain extended to include the SOL [13] show the wave amplitude in the SOL

growing to large values when the SOL density exceeds the cutoff density in front of the antenna [14]. We believe that NSTX-U discharges can be tailored to achieve efficient HHFW heating, as there have been several instances of successful HHFW operation, including record-high T_e obtained from HHFW-only discharges [15], and plasmas that are up to 70% non-inductive [16].

We have developed a cylindrical cold-plasma model to identify scenarios where significant wave power is trapped in the edge plasma. The model lacks many details included in full-wave codes but provides a simplified framework for studying wave propagation across a steep-edge density gradient. We previously identified a peculiar class of modes, called annulus resonances (AR), that have enhanced loading resistance and propagate significant power at the edge [17]. They are thus strong candidates for explaining edge losses in NSTX, and the present paper studies the influence of ARs on the reconstructed wave fields. The role of the slow wave in ARs is minimal, contrary to the common perspective that the slow wave plays a major role in interactions between the edge plasma and ICRF systems [18].

This paper is structured as follows. Section 2 describes the model and the parameters chosen to represent NSTX discharges. Section 3 explores properties of the AR with respect to m, the azimuthal mode number. In section 4, the impact of the AR on the wave field reconstruction is evaluated for a scan of the edge density. We find instances where the annulus-resonant modes dominate the spectrum and over half the wave power is trapped at the edge. We find other instances where the annulus-resonant modes are less dominant and over 80% of the wave power propagates in the core. Despite this, the scaling of the edge power percentage with the edge density obtained in the model does not always match experimental trends, and section 5 discusses the potential influence of field pitch on this discrepancy.

2. Description of the model and the choice of parameters

The model geometry, illustrated in figure 1, consists of three radial regions: a core plasma, a lower-density annulus, and an outer vacuum region. The annulus region represents the SOL, and the vacuum region represents the extremely low density region behind the limiter and inside the antenna box. The core extends to radius r_c with constant density n_c. The annulus extends from $r = r_c$ to r_a with constant density n_a. The vacuum region extends from $r = r_a$ to a conducting wall of radius r_w. The two-step density profile surrounded by vacuum is a coarse approximation of the actual density but is partially justified on the basis that SOL density profiles are relatively steep near the separatrix but become nearly flat in the mid-to-far SOL [19, 20]. The perpendicular wavelength of the fast wave in the SOL is shortest around 7 cm and is typically much longer; therefore, approximating a gradient of scale length of 1–2 cm [21] as a step function is not unreasonable. A uniform axial magnetic field is used throughout. The use of a uniform axial magnetic field is partially justified since the focus of our study is the SOL, of which the magnitude and direction of the magnetic field do not change appreciably, at least not as much as the density. The larger error comes from neglecting the poloidal field, which is substantial in NSTX. Field angles $\tan^{-1}(B_{pol}/B_{tor})$ up to 40° have been measured during HHFW experiments. The potential impact of this sizable tilt is discussed in section 5, but we note that large RF field amplitudes were observed in simulations using only a toroidal field [22]. The antenna is modeled as current straps in the θ direction at $r = r_s$ with a Faraday screen at $r = r_F$.

We choose values for the model parameters that resemble NSTX discharges as much as possible. For the radii, we use a core radius of $r_c = 0.88$ m, an annulus outer radius of $r_a = 0.915$ m, a Faraday screen radius of $r_F = 0.9315$ m, and a wall radius of $r_w = 0.9715$ m. The model core radius is chosen to keep the plasma cross-section area roughly the same as shot 120740, yielding an effective circular radius of 0.88 m. The annulus width $r_a - r_c$ is chosen to be 3.5 cm based on average values of the experimental 'outer gap' as determined from equilibrium magnetics for the L-mode discharges studied in [6]. The distance from the edge of the annulus to the Faraday screen is fixed at 1.65 cm, the distance between the outer boron nitride limiter and the Faraday screen on the midplane. The distance from the Faraday screen to the antenna strap is likewise fixed at 2 cm, as is the distance from the antenna to the vacuum wall. Also, we fix the core density at $n_c = 5 \times 10^{19}$ m^{-3}, the frequency at $f = 30$ MHz, and the equilibrium magnetic field at $B = 0.32$ T (approximate field at the edge for a 0.55 T on-axis field) for all calculations made in this paper.

A 'mode' refers to a global solution which satisfies the wave equation in each region and is matched at interfaces. Modes assume the form $E_z(r,\theta,z) = \tilde{E}_z(r,m,k_\parallel)\exp(im\theta + ik_\parallel z - i\omega t)$, based on Fourier analysis in the axial and azimuthal directions. With $k_\parallel$ given, $k_\perp$ is fixed in each region by the plasma regions by the cold-plasma dispersion: we use the notation $k_{\perp,c}^{fast}$ and $k_{\perp,c}^{slow}$ for the fast/slow-wave $k_\perp$ in the core and the corresponding notation $k_{\perp,a}^{fast}$ and $k_{\perp,a}^{slow}$ in the annulus. The slow-wave and vacuum $k_\perp$ are always cut off. The radial RF field profiles are obtained by the method detailed in [23]. Each region admits four independent solutions. In plasma, there are two fast-wave solutions and two (cutoff) slow-wave solutions; in vacuum there are exponentially decaying and growing E_z (transverse magnetic) and H_z (transverse electric) modes. By specifying the boundary conditions at each interface, a system of equations is developed, whose simultaneous solution only exists when a determinant, denoted by the function $F(k_\parallel)$, vanishes, as described in [17]. As might be anticipated for oscillation in a bounded system, the roots of $F(k_\parallel)$ are such that an integral number of half wavelengths occur in the radial profile of E_θ. Thus, we can label modes with two numbers, (m,n), with m denoting the azimuthal wavenumber and n the radial mode number. Because the fast-wave dispersion gives $k_\perp$ as a decreasing function of $k_\parallel$, lower n corresponds to larger $k_\parallel$.

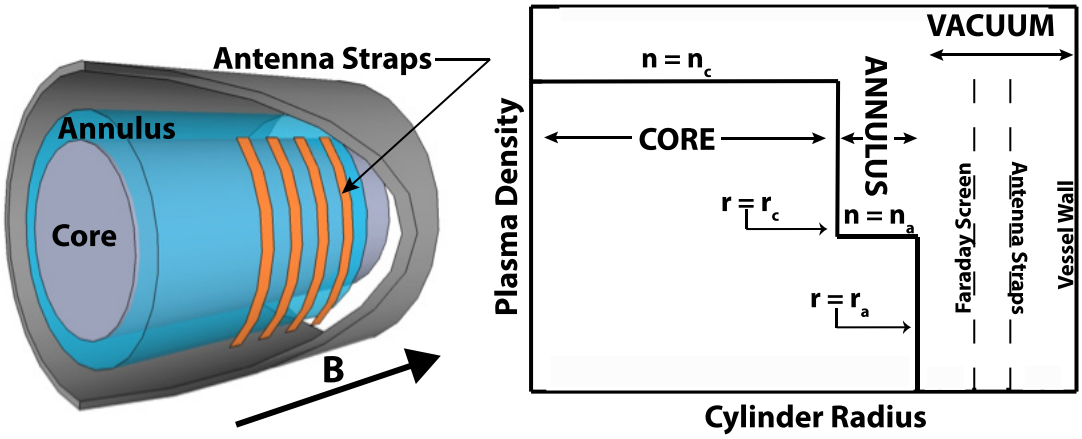

Figure 1. (*a*) Illustration of the model showing the two-step density profile and orientation of the antenna straps. (*b*) Radial density profile (not to scale) along with radial position of antenna.

The total wave fields excited by the antenna can be expressed as a sum of the modes described above. The total wave fields are obtained by the inverse Fourier transform:

$$E_\theta = \sum_m \int \tilde{E}_\theta(r,m,k_\parallel)\tilde{J}_{\rm ant}(m,k_\parallel)\mathrm{e}^{\mathrm{i}m\theta+\mathrm{i}k_\parallel z}\mathrm{d}k_\parallel. \quad (1)$$

In equation (1), $\tilde{J}_{\rm ant}(m,k_\parallel)$ is the antenna spectral current density and $\tilde{E}_\theta$ is the azimuthal electric field per unit antenna spectral current density. For any $k_\parallel$ not equal a root of $F(k_\parallel)$, $\tilde{E}_\theta(r,m,k_\parallel)$ has a discontinuity at the antenna strap radius associated with an infinite current sheet of unit magnitude and wavenumber $k_\parallel$. The expression for $\tilde{E}_\theta$ contains $F(k_\parallel)$ in the denominator, so that the integral reduces to a sum of residues, one for each pole. The amplitude of each mode is thus given by two factors: (i) the amplitude of $\tilde{J}_{\rm ant}(m,k_\parallel)$ at the $k_\parallel$ and m of the mode, and (ii) the size of the residue, which is proportional to $(\mathrm{d}F(k_\parallel)/\mathrm{d}k_\parallel)^{-1}$. The latter is a property inherent to the mode and independent of antenna geometry; indeed, we could study the 'bare' or 'unweighted' amplitude of modes by using a uniform antenna spectrum (e.g. a delta-function excitation $J_{\rm ant} = I_0\delta(z)\delta(\theta)$). As described in [17], the large amplitude of an AR is due to a near vanishing of $\mathrm{d}F(k_\parallel)/\mathrm{d}k_\parallel$ independent of the particulars of the antenna configuration.

The antenna strap current distribution is modeled as 12 infinitely thin filaments. The Fourier spectrum in the axial direction is therefore a sum of 12 plane waves. Given that the height of the antenna straps is 68.9 cm, and using the effective plasma radius above, we approximate the antenna angular span as 0.724 radians in the model. We assume a uniform current distribution in the azimuthal (poloidal) direction due to the long vacuum wavelength compared to the strap length. Given a phase difference of ϕ between straps, a strap spacing of d, a current for each strap of I_0 and an angular span of α,

$$J_{\rm ant}(r,\theta,z) = I_0\delta(r-r_{\rm a})\left[\Theta(\theta+\alpha/2)-\Theta(\theta-\alpha/2)\right] \times \sum_{i=0}^{12}\delta(z+(11-2i)d/2)\mathrm{e}^{-\mathrm{i}\phi(11-i)/2} \quad (2)$$

where Θ is the Heaviside step function. $J_{\rm ant}$ can be decomposed into a Fourier series in the azimuthal direction and a Fourier transform in the axial direction:

$$\tilde{J}_{\rm ant}(r,m,k_\parallel) = I_0\delta(r-r_{\rm a})\tilde{J}_\theta(m)\tilde{J}_\parallel(k_\parallel) \quad (3)$$

$$\tilde{J}_\theta(m) = \frac{\sin(m\alpha/2)}{m\pi} \quad (4)$$

$$\tilde{J}_\parallel(k_\parallel) = \sum_{i=0}^{12}\mathrm{e}^{\mathrm{i}k_\parallel(11-2i)d/2}\mathrm{e}^{-\mathrm{i}\phi(11-i)/2}. \quad (5)$$

We note that $\tilde{J}_\theta$ scales as $1/m$ and is nearly zero whenever $m\alpha/2$ is an integer multiple of π. This clearly favors low-m modes. On the other hand, $\tilde{J}_\parallel$ peaks around $k_\parallel = \phi/d$. For NSTX, $d = 21.5$ cm, and typically phasings are $\pi/6$, $\pi/2$ and $5\pi/6$. This model clearly ignores (i) the finite width of the antenna straps, (ii) the radial feeds, (iii) the effects of the sidewalls [24], and (iv) changes in current along the length of the straps.

In this paper, the term 'mode amplitude' refers to the amount of wave power a mode conducts axially along the cylinder. We denote the amplitude of the (m,n) mode as $P_{m,n}$ but will also express this as a loading resistance $R_{m,n}$ defined by $R_{m,n}I_0^2/2 = P_{m,n}$, with I_0 defined in equation (2). $P_{m,n}$ can be calculated by two methods. First, we compute the power output of the antenna, P, using the induced EMF method [25]:

$$P = \int \langle \mathbf{E}\cdot\mathbf{J}_{\rm ant}\rangle\,\mathrm{d}V, \quad (6)$$

where $<\ldots>$ denotes the time-averaging of complex quantities. Using equation (1), this can be expressed as

$$P = \frac{1}{2}(2\pi)^2 r_{\rm s}\sum_m\int \tilde{E}_\theta(r,m,k_\parallel)\left|\tilde{J}_{\rm ant}(m,k_\parallel)\right|^2\mathrm{d}k_\parallel. \quad (7)$$

Again, the integral over $k_\parallel$ reduces to a sum of residues, each term being the individual mode power. Equivalently, P can be computed by integrating the axial Poynting flux over the cross-section of the cylinder, and the orthogonality of modes allows this expression to be written as a sum of individual Poynting fluxes for each mode:

$$P_{m,n} = \int_{r=0}^{r=r_w} \int_{\theta=0}^{\theta=2\pi} \hat{z} \cdot \left\langle \tilde{\mathbf{E}}(r,m,k_\parallel) \times \tilde{\mathbf{H}}(r,m,k_\parallel)^* \right\rangle r\mathrm{d}r\mathrm{d}\theta. \quad (8)$$

Equation (8) is independent of the axial position z, and both equations (7) and (8) yield the same result, as expected for a system without dissipation. Similar to the discussion of mode amplitudes given below (equation (1)), the individual loading resistance of each mode is determined by (i) the antenna spectral power at the wavenumber of the mode and (ii) the amplitude of the residue. In this paper, we use the term 'bare' or 'unweighted' loading resistance to denote loading obtained with a uniform antenna spectrum, $J_{\mathrm{ant}}(m,k_\parallel) = \text{constant}$.

We emphasize that this cylindrical model is a response to the need for qualitative understanding and is not intended for precise calculations of loading resistances. The model is cylindrical, so toroidal effects are clearly excluded. With a realistic magnetic-field profile, poloidal symmetry is broken, and modes of different azimuthal mode numbers m may couple, potentially transferring power from ARs to other modes. The model does not include any of the antenna structures surrounding the strap and Faraday screen; considerable research has been conducted to study the effects of such components [26], especially when they are misaligned with the magnetic field, and their possible excitation of an electric field component parallel to the background magnetic field [27]. Finite-temperature and non-linear effects are omitted, including conversion to ion Bernstein waves, parametric decay instability, and RF rectification. Indeed, no form of dissipation is included; wave energy coupled from the antenna propagates out of the ends of the cylinder without absorption. The actual mechanism converting HHFW power in the SOL to a divertor heat flux has not yet been definitively determined, but dissipation by far-field RF sheaths is a leading candidate [11]. Core absorption is the usual Landau damping and transit-time magnetic pumping, which are anticipated to be quite large for high-beta plasmas such as those found in the NSTX core [28, 29]. These hot-plasma effects may also be strong enough to substantially change the wave fields from their cold-plasma solutions found here. We presume that the high edge field amplitude of the AR will drive a high rate of edge absorption relative to core absorption once the proper SOL damping mechanism is identified and included, but this remains a crucial future step to verify by comparing core and edge damping rates. We also observe that this model treats the tokamak as a plasma-filled waveguide, whereas AORSA simulations including that of the SOL resemble a plasma-filled cavity. We emphasize again that the cylindrical model allows for relatively short computation time and faster exploration of the parameter space as well as provides the ability to resolve individual modes and to separate the contributions from fast and slow waves.

3. Properties of ARs over several azimuthal mode numbers

The AR condition is one where a half-wavelength structure in E_θ fits into the combined annulus/vacuum region, which we refer to as the 'edge' region. The modes that most nearly satisfy this condition have a greatly enhanced 'bare' or unweighted loading resistance and propagate over half of their wave power at the edge. The concept of 'bare' mode amplitude is discussed above (equation (1)). What we call 'annulus-resonant modes' are the modes, for each m, that most closely satisfy this condition and consequently have the highest bare loading resistance among all modes of the same m. Indeed, when the bare loading resistances for all modes of a single m are plotted against $k_\parallel$, the AR modes, if present, appear as a peak in an otherwise monotonically decreasing curve, as shown in figure 2. For the typical SOL parameters modeled here, one generally finds at most one AR per m. It is possible that there is no AR present, as shown in figure 2. An analytic expression for the AR condition is cumbersome due to the matching of annulus fields to vacuum fields, but we can generally understand its dependence on certain model parameters as follows. $k_\perp^{\mathrm{fast}}$ decreases with $k_\parallel$ but increases with plasma density. When plasma density in the annulus increases, the $k_\parallel$ of the AR condition decreases to keep $k_\perp^{\mathrm{fast}}$ approximately the same. Likewise, increasing the width of the annulus region decreases the $k_\parallel$ of the AR condition. Perkins *et al* [17]

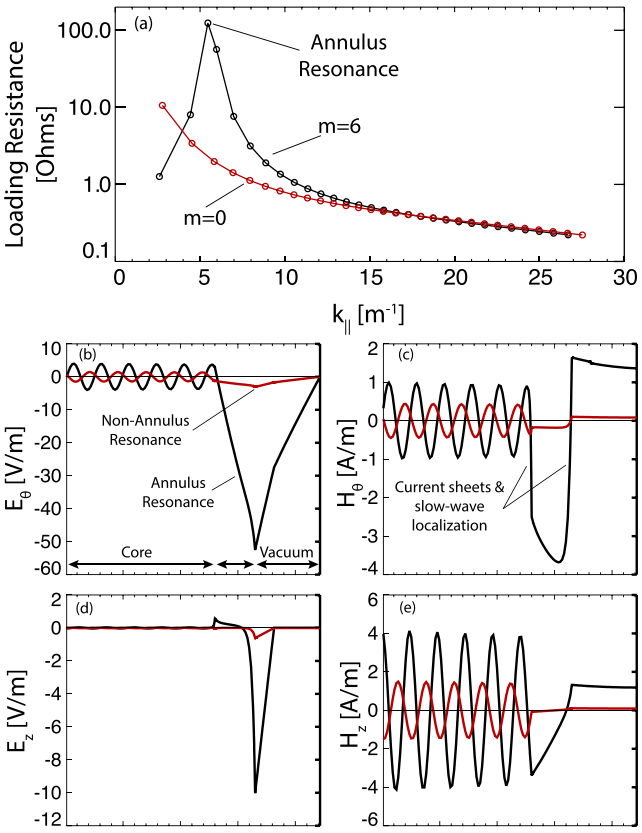

Figure 2. (*a*) Bare loading resistance for $m = 6$ (black) and $m = 0$ modes (red) for an annulus density of 1.5×10^{18} m^{-3}, showing typical loading resistance curves with and without an AR mode. (*b*)–(*e*) Field profiles for the $m = 6$ annulus resonance (black curves) and for the $m = 6$, $k_\parallel = 6.98$ m^{-1} non-annulus resonance (red curves) shown in (*a*). The difference in amplitude, especially at the edge, is clear. Also, the abrupt changes in H_θ shown in (*c*) indicate the slow-wave layers and associated axial RF currents. The modes persist even when the slow wave is removed from the model, as the axial currents become infinitely thin current sheets.

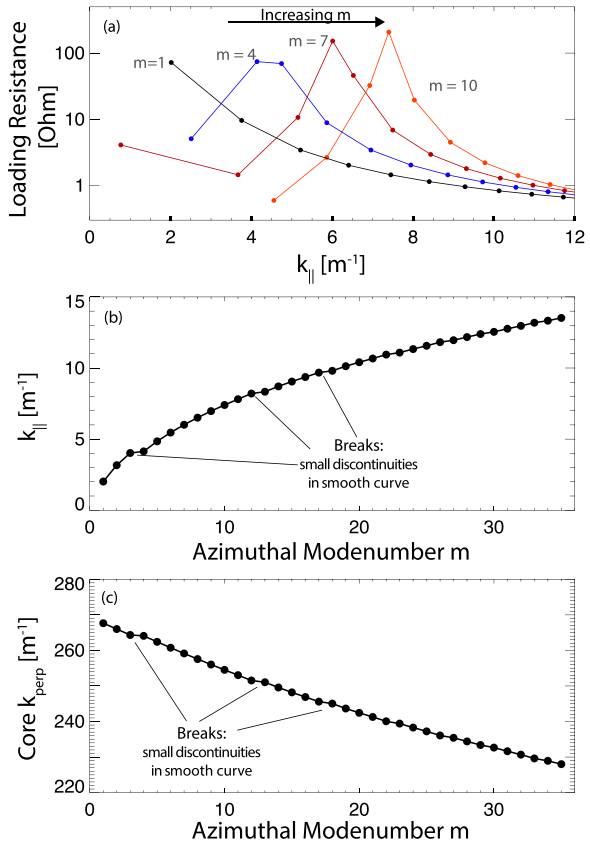

Figure 3. (*a*) Loading resistance versus $k_\parallel$ for $m = 1$ (black), $m = 4$ (blue), $m = 7$ (red), and $m = 10$ (orange) modes. The $k_\parallel$ of the AR modes increases with increasing m. (*b*) The $k_\parallel$ value of the largest mode for each m. (*c*) As in (*b*) but with $k_{\perp,c}^{\text{fast}}$ as the abscissa. $n_a = 1.5 \times 10^{18}$ m^{-3} for all three plots.

contains a more detailed discussion and figures regarding the dependence of the AR condition on these parameters.

The ARs are dominated by fast-wave fields with little contribution from the slow wave. This is mostly due to the fact that, for these parameters, the slow wave is cut off with a radial length scale of millimeters, which confines the slow wave to very narrow layers at the core–annulus and annulus–vacuum interfaces. Still, the slow wave could, in principle, be essential if it joins fast-wave solutions across the interfaces in a fashion that would otherwise violate boundary conditions without the slow-wave solution. However, inspection of the field profiles for the AR shows that removing the slow wave (making it more and more evanescent) only causes a discontinuity in H_θ at the annulus–vacuum interface, which is indicative of an infinitely thin current sheet. Hence the role of the slow wave in the AR mode is simply to broaden this current sheet by over a few millimeters, and the existence of the AR cannot be attributed to the inclusion of the slow-wave solution. We note that the slow wave may play a more prominent role at the lower hybrid resonance layer or at antenna-box components, neither of which are included in the model. However, the lower hybrid resonance density is very low for these parameters, typically 10^{16} m^{-3}, and is probably confined within the antenna box and is not expected to influence the far fields [30]. Slow-wave excitation at the antenna box may influence sputtering and heat loads but is outside the scope of the present study.

This section will focus on the behavior of AR modes for different m. As mentioned, there is typically at most one AR per m, but the $k_\parallel$ of the resonance increases with m. This is demonstrated in figure 3(*a*), where the bare loading resistance is plotted against $k_\parallel$ for select azimuthal mode numbers m. There is one AR for every m, and the $k_\parallel$ value of this peak increases with increasing m. For low enough m (in this case, $m \leqslant 0$), this peak begins to disappear into the vacuum cutoff $k_\parallel = \omega/c$. In figure 3(*b*), the $k_\parallel$ value of the largest mode for each m is plotted against m; there appears to be a functional relationship. Figure 3(*c*) is similar to figure 3(*b*) except the vertical axis is $k_{\perp,c}^{\text{fast}}$, the fast wave $k_\perp$ in the core. This last plot appears piecewise linear with 'breaks', consecutive modes that have similar $k_{\perp,c}^{\text{fast}}$.

Figure 3(*b*) is important to understand. The 'trajectory' of the AR condition through the $k_\parallel - m$ space determines whether or not these modes will intercept the peaks in the antenna spectrum. It is also important to understand how parameters such as the magnetic field and annulus density affect this 'trajectory'.

3.1. Mode spacing

In section 2, we introduce the radial mode number n as the number of zeros in the radial profile of E_θ. We now derive approximate analytic expressions for the $k_\parallel$ spacing between modes of consecutive n and fixed m and between those of consecutive m and fixed n. Most of the zeros in the radial E_θ profile occur in the core because the core is the largest region and also because $k_\perp^{\text{fast}}$ is relatively large there due to the high density. The core fast-wave fields are linear combinations of the Bessel functions $J_m(k_{\perp,c}^{\text{fast}}(m,n)r)$ and $J_{m+1}(k_{\perp,c}^{\text{fast}}(m,n)r)$, where the notation $k_{\perp,c}^{\text{fast}}(m,n)$ denotes the value of $k_{\perp,c}^{\text{fast}}$ for a mode of azimuthal number m and radial mode number n. The Bessel functions can be approximated by their asymptotic forms:

$$J_m(k_{\perp,c}^{\text{fast}}(m,n)r) \approx \cos\left(k_{\perp,c}^{\text{fast}}(m,n)r - m\frac{\pi}{2} - \frac{\pi}{4}\right). \quad (9)$$

If we define $\phi_{m,n}$ as the phase argument in equation (9),

$$\phi_{m,n} \approx k_{\perp,c}^{\text{fast}}(m,n)r - m\frac{\pi}{2} - \frac{\pi}{4}, \quad (10)$$

then $\phi_{m,n}$ is an approximation to the fast-wave phase at the core–annulus boundary. We then conjecture that $\phi_{m,n+1}$ is greater than $\phi_{m,n}$ by a value of π to produce an extra zero in the radial profile of E_θ in the core (a similar analysis is used in [31]). Then

$$k_{\perp,c}^{\text{fast}}(m,n+1) = k_{\perp,c}^{\text{fast}}(m,n) + \frac{\pi}{r_c}. \quad (11)$$

Similarly, we conjecture that $\phi_{m+1,n} \approx \phi_{m,n}$, since both modes have the same number of zeros. This conjecture leads to

$$k_\perp^{\text{fast}}(m+1,n) = k_\perp^{\text{fast}}(m,n) + \frac{\pi}{2r_c}. \quad (12)$$

Increasing $k_{\perp,c}^{\text{fast}}$ means decreasing $k_\parallel$. In either case, changes in $k_\parallel$ are found by solving the fast-wave dispersion:

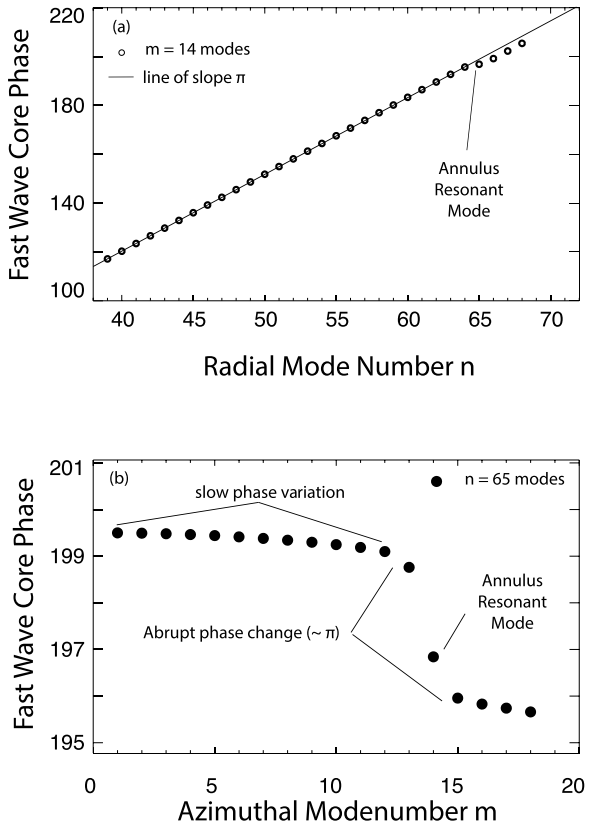

Figure 4. (*a*) Core phase $\phi_{14,n}$ for the $m = 14$ mode as a function of n. A straight line with slope π is drawn for reference. (*b*) Core phase $\phi_{m,65}$ for the $n = 65$ radial mode as a function of m; note the change in vertical scale. For both figures, $n_a = 1.5 \times 10^{18}$ m^{-3}.

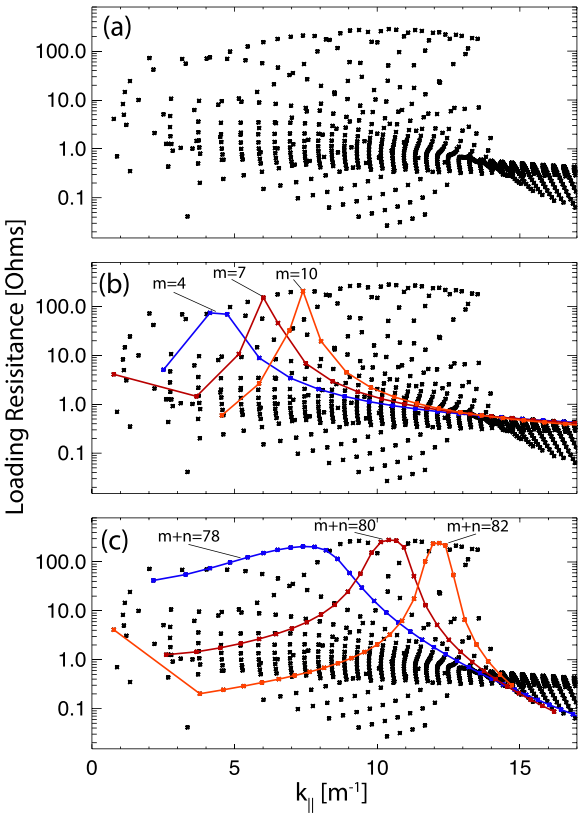

Figure 5. (*a*) Scatter plot of loading resistance versus $k_\parallel$ for all modes. (*b*) Same as (*a*) with $m = 4$ (blue), $m = 7$ (red), and $m = 10$ (orange) modes joined by colored lines. (*c*) Same as (*a*) with $m + n = 78$ (blue), $m + n = 80$ (red), and $m + n = 82$ (orange) modes joined by colored lines.

$$n_\perp^2 = \frac{(R - n_\parallel^2)(L - n_\parallel^2)}{S - n_\parallel^2} \tag{13}$$

with n denoting the refractive index $n = ck/\omega$.

Both conjectures assume that any change in radial phase between modes occurs primarily in the core and that the phase change in the combined annulus–vacuum region is small. The impact of the phase change will be shown below. We acknowledge that the term 'radial phase' is a poorly defined concept for the edge; the wave fields are radially cut off in the vacuum and sometimes also in the annulus. Moreover, discontinuous jumps in phase occur at sharp interfaces such as the ones used in this model.

We now compare the predictions made by equations (11) and (12) to the modes computed by the model. Figure 4(*a*) plots the asymptotic core fast-wave phase for $m = 14$ modes, $\phi_{14,n}$, as a function of n. The resulting plot is remarkably linear with slope π as predicted above. At $n = 65$, there is a joggle in the linear trend. The $n = 65$, $m = 14$ mode is an AR and will be discussed below. Figure 4(*b*) plots $\phi_{m,65}$ versus m from $m = 1$ to $m = 18$; for larger m, the AR disappears into the vacuum cutoff $k_\parallel = \omega/c$. For $m < 14$, the curve is very flat; the percent change in $\phi_{m,65}$ from $m = 1$ to $m = 13$ is 0.37%. This insensitivity of $\phi_{m,n}$ to n is consistent with equation (12). The deviation from flatness is likely due to the much smaller variation in phase across the annulus/vacuum regions.

Like figure 4(*b*), there is an abrupt change in phase at AR $m = 14$, $n = 65$. AR modes have a unique fast-wave phase at the core–annulus boundary; whereas most other modes have a phase separation of π, AR modes are separated by approximately $\pi/2$ from their nearest neighbors (nearest in $k_\parallel$) [17]. This explains the abrupt phase change in both figures.

If the plot in figure 4 is extended to $m < 1$, the phase $\phi_{m,65}$ will increase linearly. This, however, is an artifact of the asymptotic phase $\phi_{m,n}$. Because $J_{-m}(x) = (-1)^m J_m(x)$ for integral m, the negative m modes exhibit behavior similar to that of their positive counterparts.

3.2. Mode families and the AR condition

This section explains the piecewise linear dependence of the $k_{\perp,c}^{\text{fast}}$ of annulus-resonant modes versus m seen in figure 3. Figure 5(*a*) is a scatter plot of loading resistance versus $k_\parallel$ for all modes from $m = 0$ to $m = 40$. Figure 5(*a*) is similar to figure 3 but has a logarithmic vertical scale, more azimuthal mode numbers, and no coloring to distinguish the m values of the modes. These annulus-resonant modes lie at the top of this figure; the abrupt end of these modes at $k_\parallel \approx 14$ m^{-1} is due to the truncation of higher-m modes at $m = 40$. Certain sets of modes appear to lie on smooth curves in figure 5; these curves rise to a crest and then decrease with increasing $k_\parallel$, with the

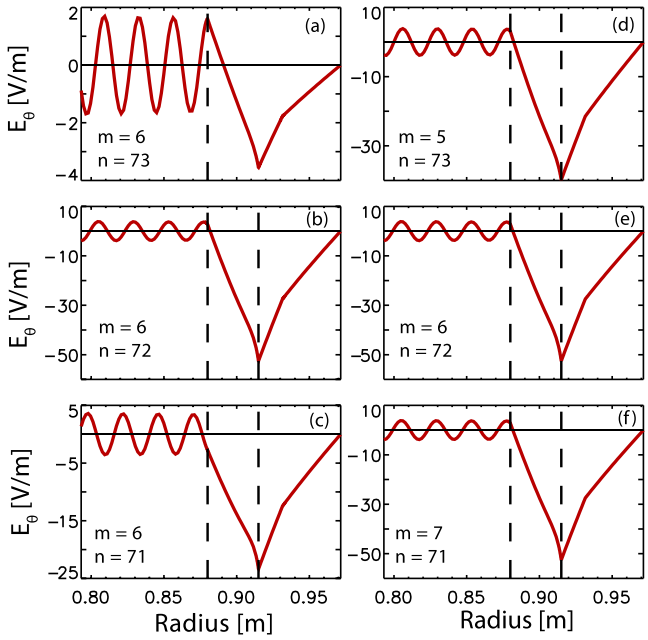

Figure 6. Radial profiles of E_θ for various modes. In the left column, m is fixed at $m = 6$ and n decreases by one down the panels. In the right column, m increases by one while n decreases by one down the panels.

envelope of these curves being the set of annulus-resonant modes. These smooth curves are not defined by modes of the same m value; figure 5(b) demonstrates this by repeating the scatter plot with modes of the same m joined by colored curves. Here, the smooth curves are defined by all modes whose sums of $m + n$ are equal; we refer to such sets as families. In figure 5(c), modes with equal $m + n$ are joined by colored lines to differentiate families. For the simulation used for figure 5, the $m + n = 78$ family is the dominant family for $k_\parallel$ between 4 and 8 m^{-1} and contains the AR modes for $m = 4$ to $m = 12$. Above $k_\parallel \approx 8\ \mathrm{m}^{-1}$, the loading resistance of the $m + n = 78$ family declines as the loading of the $m + n = 79$ family increases. The AR modes between $k_\parallel = 8\ \mathrm{m}^{-1}$ and $k_\parallel = 9.7\ \mathrm{m}^{-1}$ belong to the $m + n = 79$ family. The transition of maximal loading between families is emphasized by the $m = 4$ modes, colored blue in figure 5(b). The AR peak in loading resistance for these modes is broader than usual (compare the $m = 4$ modes to the $m = 7$ and $m = 10$ modes in the same figure, or to figure 2). This peak consists of two closely spaced and nearly equal modes, each coming from a different family as the AR condition transitions from the $m + n = 77$ curve to the $m + n = 78$ curve.

Within a family, the outermost half wavelength varies relatively slowly across modes. Figure 6 shows this variation for two cases: for fixed m and varying n, and for fixed $m + n$. In the left-hand panels, m is fixed at 6, and n decreases by one from 73 (figure 6(a)) to 72 (figure 6(b)) to 71 (figure 6(c)). The outermost half wavelength grows and sweeps across the annulus–core boundary. The $n = 72$ mode most nearly satisfies the AR condition and correspondingly has the largest amplitude. In the right-hand panels of figure 6, n decreases by one and m increases by one, going from $m = 5$ and $n = 73$ (figure 6(d)) to $m = 6$ and $n = 72$ (figure 6(e)) to $m = 7$ and $n = 71$ (figure 6(f)). The outermost half wavelength now varies almost imperceptibly and closely satisfies the AR condition. As one continues to increment m and decrement n keeping $m + n$ constant, the outermost half wavelength eventually grows longer than the edge width, losing the AR condition and leading to a falloff in mode amplitude. However, as the $m + n = 78$ family falls off, the $m + n = 79$ family begins to satisfy the AR condition more closely. It is currently not clear why holding $m + n$ constant slows the variation of the width of the outermost half wavelength.

The dependence of the $k_{\perp,\mathrm{c}}^{\mathrm{fast}}$ and $k_\parallel$ of the AR on m, figures 3(c) and (b) respectively, can be obtained by applying equation (12) within a family, so that $m + n =$ constant:

$$k_{\perp,\mathrm{c}}^{\mathrm{fast}}(m+1, n-1)r_\mathrm{c} = k_{\perp,\mathrm{c}}^{\mathrm{fast}}(m,n)r_\mathrm{c} - \frac{\pi}{2}, \qquad (14)$$

from which the $k_\parallel$ dependence follows from the fast-wave dispersion, equation (13). Increasing m within a family decreases $k_{\perp,\mathrm{c}}^{\mathrm{fast}}$ and increases $k_\parallel$. Equation (14) is only valid within a family; when the AR condition transitions from one family to the next, there exists a discontinuity in $k_{\perp,\mathrm{c}}^{\mathrm{fast}}$, which explains the piecewise linear behavior seen in figure 3(c).

4. The role of ARs in wave field reconstructions

In this section, we evaluate the role that AR modes play in wave field reconstructions, anticipating that strong excitation of AR modes will result in a large fraction of the total wave power being localized in the edge. The excitation of AR modes, relative to non-AR modes, depends on how closely the $k_\parallel$ and m values of the AR modes match the spectral peaks of the antenna spectrum. Thus, the dependence of the $k_\parallel$ of AR modes for different m studied in section 3 (see figure 3) plays a central role: it defines the 'trajectory' of the AR modes through the $k_\parallel - k_\theta$ plane and how closely it overlaps with the antenna spectral peak. Because the AR modes have a very high unweighted loading resistance (see discussion under equation (1)), we expect that, when this trajectory intercepts the antenna spectral peak, the AR modes will dominate the non-AR modes in the wave field reconstructions.

Section 4.1 develops the mathematics for how wave power is partitioned between different regions in the model and defines the amount of power that is exchanged between the core and edge regions. Sections 4.2 and 4.3 present loading resistance calculations for an inter-strap antenna phasing of $\pi/2$ and $5\pi/6$ respectively for various annulus densities, with the core density kept fixed. While quantitative results are presented, we emphasize the qualitative behavior of the AR modes and their k value relative to the antenna spectrum. We find instances where (i) the AR modes account for a large fraction of the total wave power, and (ii) a large fraction of the total wave power, over 50%, is 'trapped' at the edge. Indeed, the two features are fairly well-correlated, as expected. We also find instances where the percentage of core loading is much larger, around 80%, and where the power at the edge can propagate into the core. These findings are a

Table 1. Loading resistance by region and the contribution of AR modes for each n_a. The left-hand columns show the total loading, its partition into edge and core power, and the power that oscillates between the core and edge (equation (15)). In the right-hand columns, 'total' denotes the percent contribution of the AR modes to the total loading, while the 'edge' and 'core' columns denote the percent contribution to each region. For instance, 97% in the 'edge' column means that the AR edge power is 97% of the total edge power.

Annulus Density	Loading resistance (Ω)				AR loading		
	Total	Core (%)	Edge (%)	Oscillating	Core (%)	Edge (%)	Total (%)
0.5×10^{18}	2.31	1.02 (44%)	1.29 (56%)	0.21	14	97	60
1.0×10^{18}	3.96	1.91 (48%)	2.04 (52%)	0.74	27	94	63
1.5×10^{18}	3.93	2.68 (68%)	1.25 (32%)	0.85	23	81	42
2.0×10^{18}	5.58	4.18 (75%)	1.41 (25%)	1.31	19	76	34

promising explanation for the edge loss of HHFW power in NSTX. However, the case of $\pi/2$ phasing shows the *opposite* trend of fraction edge loading with increasing annulus density—namely, in this model, power trapping at the edge tends to decrease with increased annulus density. In the $5\pi/6$ phasing case, though, the power trapping is observed to initially increase with annulus density. The discrepancy between the model and the experimental results may be explained by magnetic pitch, as discussed in section 5.

4.1. The partition of wave power between core and edge

The expression for the time-averaged (active) Poynting flux Γ_z through a surface normal to the axial direction is given as a double sum over all modes:

$$\langle \Gamma_z \rangle = \sum_{m,n,m',n'} \int\int \langle \tilde{E}_r(r,m,n)\tilde{H}^*_\theta(r,m',n') - \ldots \tilde{E}_\theta(r,m,n)\tilde{H}^*_r(r,m',n') \rangle \, \mathrm{e}^{\mathrm{i}(k_\parallel - k'_\parallel)z + \mathrm{i}(m-m')\theta} r\mathrm{d}r\mathrm{d}\theta.$$

In this sum, $k_\parallel$ is the axial wavelength for the (m,n) mode, and $k'_\parallel$ is for the (m',n') mode. The cross-terms indicate interference between modes. When integrating over the entire azimuthal angle, we can apply orthogonality between the two azimuthal mode numbers m and m'. When integrating over the entire radial domain, we have the orthogonality of n and n'. In the case of both, the expression for axial wave power reduces to the sum of individual fluxes from each mode, each of which is axially constant with no interference between modes.

When integration occurs over the entire azimuthal angle but not over the entire radial domain, the Poynting flux becomes

$$\langle S_z \rangle = 2\pi \sum_{m,n,n'} \int \langle \tilde{E}_r(r,m,n)\tilde{H}^*_\theta(r,m,n') - \ldots \tilde{E}_\theta(r,m,n)\tilde{H}^*_r(r,m,n') \rangle \, \mathrm{e}^{\mathrm{i}(k_\parallel - k'_\parallel)z} r\mathrm{d}r.$$

For each m, these terms are categorized as either diagonal terms ($n = n'$) or cross-terms ($n \neq n'$). Diagonal terms do not have z dependence, but cross-terms do. If we integrate over the core, then the diagonal terms define a fixed amount of power that remains in the core, but each cross-term describes a power flux between the core and the edge that varies sinusoidally with z. We refer to this as 'oscillating' power, which should not be confused with reactive (time-oscillating) power. Likewise, when integrating over the edge, the diagonal terms describe power that remains at the edge, which we refer to as

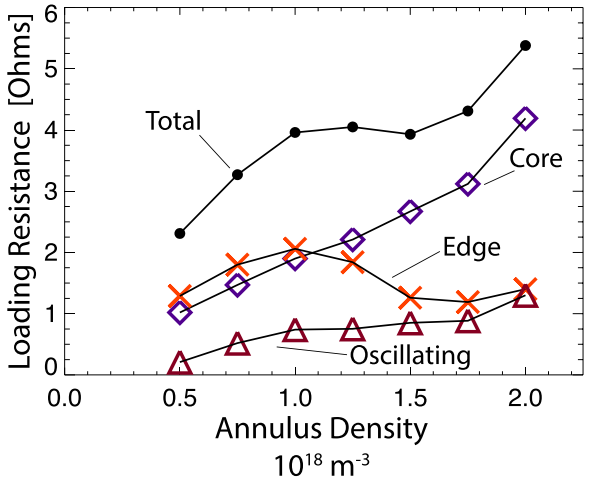

Figure 7. Trend in loading resistance as n_a increases: circles, total loading; diamonds, core loading; crosses, edge loading; triangles, oscillating power.

'trapping' at the edge. The oscillating power must be computed numerically at each z location of interest. A convenient and z-independent metric of the power available for oscillation is

$$P_{\mathrm{osc}} = 2\pi \sum_{n \neq n'} \left| \int \langle E_r(r,m,n)H^*_\theta(r,m,n') - \ldots E_\theta(r,m,n)H^*_r(r,m,n') \rangle \right| r\mathrm{d}r. \quad (15)$$

Note that no power oscillates between modes of different m values. Also, if there is one dominant mode for a given m, then the oscillating power will be a small fraction of the total wave power contained in these m modes.

4.2. Current-drive phasing

The results of changing the annulus density n_a in the range of 5.0×10^{17} to 2.0×10^{18} m^{-3} are summarized in table 1 and shown graphically in figure 7. The general trend with increasing n_a over this density range is that (i) the total loading increases, (ii) fractional loading to the core increases, and (iii) the percent contribution of the AR modes decreases. The increase in total loading with n_a results from increases in both AR and non-AR modes. Non-AR loading steadily increases with increasing n_a, which improves core loading. Meanwhile, AR loading does not monotonically increase with n_a for the reasons discussed below, and the AR contribution decreases

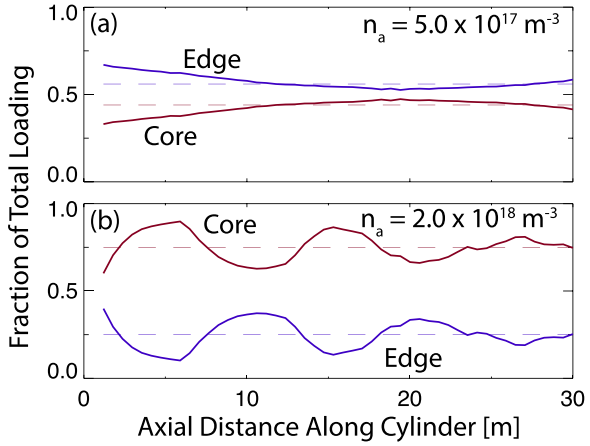

Figure 8. Percentage of power contained in the core (red) and edge (blue) as a function of axial distance from the antenna. Dashed lines indicate a fixed percentage of power (section 4.1). (*a*) $n_a = 5.0 \times 10^{17}$ m^{-3}, and (*b*) $n_a = 2.0 \times 10^{18}$ m^{-3}.

as n_a rises. Also, the amount of power that oscillates between the edge and the core, equation (15), steadily increases from a small fraction (∼10%) to nearly the full power at the edge. We might say that the power at the edge is no longer trapped there. Figure 8 plots the percent loading in the core and edge as a function of z moving away from the antenna. For $n_a = 5.0 \times 10^{17}$ m^{-3} (figure 8(*a*)), the oscillating power is low, and the edge power is close to its fixed value. For $n_a = 2.0 \times 10^{18}$ m^{-3} (figure 8(*b*)), the power at the edge is lower, and a greater portion of it can propagate into the core. Absorption is not included in this model, but is predicted to be strong for NSTX core plasmas [29]; we expect that any wave power that penetrates the core will be absorbed there.

A more detailed perspective is afforded by figures 9(*a*) and (*b*). Each figure contains a contour plot of the antenna spectral power on the $k_\parallel - k_\theta$ plane. k_θ is given as m/r_a. Each contour line denotes a factor-of-two change in spectral power. Each circle denotes a mode, with lighter colors signifying a higher loading resistance. Only the 50 largest modes are plotted for clarity; these modes account for about 90% of the total wave power. The diamonds denote the locations of the AR modes; as a set, the AR modes take a curved trajectory through the $k_\parallel - k_\theta$ plane. Since the AR modes have a high unweighted loading resistance, one could think of this AR trajectory as a ridgeline of the $k_\parallel - k_\theta$ plane. A diamond filled with a circle denotes an AR mode that is in the top 50 modes. At $n_a = 1.0 \times 10^{18}$ m^{-1} (figure 9(*a*)), the AR ridge lies directly on top of the first azimuthal sideband, with $m = 12$ being the strongest AR mode excited. This explains the relatively strong contribution of the AR modes for this density. Many non-AR modes lie in the primary antenna spectral peak. In figure 9(*b*), increasing n_a to 1.75×10^{18} m^{-3} moves the AR ridge off the sideband. At the peak of the axial spectrum ($k_\parallel = 7.3$ m^{-1}), the AR ridge lies near the node in the azimuthal spectrum at $m = 8$. This explains the non-monotonic behavior of AR loading (figure 7). Also, for the strongest AR modes at $m = 5$, $m = 6$, and $m = 7$, neighboring modes of the same m are also strongly excited. With several large modes of the same m, the power oscillating between the core and edge increases because, as explained in section 4.1, this oscillation is caused by interference of modes of the same m. As evidenced in figure 9(*a*), typically there is only one mode strongly excited at each m in the case of $n_a = 1.0 \times 10^{18}$ m^{-3}.

For the set of AR modes, the fraction of power conducted at the edge decreases from 86% at $n_a = 5.0 \times 10^{17}$ m^{-3} to 56% at $n_a = 2.0 \times 10^{18}$ m^{-3}. This is because higher-m AR modes conduct more power at the edge. Increasing the annulus density moves the AR ridge to the right in the $k_\parallel - k_\theta$ space, decreasing the m value at which the AR trajectory intercepts the antenna $k_\parallel$ peak at $k_\parallel = 7.3$ m^{-1}; see figure 10.

4.3. $5\pi/6$-phasing: heating phasing

For the NSTX antenna, $5\pi/6$ inter-strap phasing avoids a phase discontinuity between the sixth and seventh straps that would occur for π phasing [32]. For $5\pi/6$ phasing, the primary axial spectrum peaks at $k_\parallel = 12.2$ m^{-1}. There is a second peak at $k_\parallel = -22$ m^{-1}, but the coupling to modes at such large $|k_\parallel|$ is weak enough to ignore. Table 2 and figure 11 show the loading calculations for this phasing. The total loading is reduced by roughly a factor of three compared to that of $\pi/2$ phasing but does steadily increase as n_a increases. Similarly, the core loading increases with n_a but at a slower rate than the $\pi/2$ case. The percentage of power at the edge is substantially smaller than that with $\pi/2$ phasing but is still significant, around one third of the total power. In contrast to the decrease in percent edge loading with n_a seen for $\pi/2$ phasing, the percent edge loading for $5\pi/6$ phasing rises as n_a is raised from 0.5 to 1.0×10^{18} m^{-1}, but levels off in the range of 1.0 - 2.0×10^{18} m^{-1}. In this latter range of n_a, the power available to oscillate between the edge and core increases substantially. The behavior of edge loading versus n_a is a monotonic increase, which contrasts with the $\pi/2$ case and will be discussed below. The percent contribution of the AR modes is similar to the percent edge loading; for $n_a = 0.5$ and 1.0×10^{18} m^{-3}, it is substantially lower than that in the $\pi/2$ case but rises instead of decreases with n_a.

Figures 9(*c*) and (*d*) show the $n_a = 1.0 \times 10^{18}$ m^{-3} and 2.0×10^{18} m^{-3} cases on the $k_\parallel - k_\theta$ plane. At $5\pi/6$ phasing, the AR trajectory now intercepts the axial peak in the antenna spectrum, $k_\parallel = 12.2$ m^{-1}, at substantially higher k_θ than in the $\pi/2$ case. For $n_a = 1.0 \times 10^{18}$ m^{-3} (figure 9(*c*)), the strongest modes are the $m = 30$, 31, and 32 AR modes, with relatively strong contributions from the $m = 38$ and 39 AR modes, whereas for $\pi/2$ phasing the strongest modes are the $m = 11$, 12, and 13 AR modes. For $n_a = 2.0 \times 10^{18}$ m^{-3} (figure 9(*d*)), the strongest modes are the $m = 22$ and 23 AR modes, whereas for $\pi/2$ phasing the strongest modes are the $m = 5$, 6, and 7 AR modes. It is remarkable that these AR modes are the dominant modes in this case; they lie on the relatively weak third and fourth azimuthal sidelobes of the antenna spectrum but have a high 'bare' loading resistance (a concept discussed below equation (1)). This is in contrast to the non-AR modes that lie directly on top of the main antenna spectral peak but have relatively low bare loading resistances. However, since the azimuthal spectral weighting of the

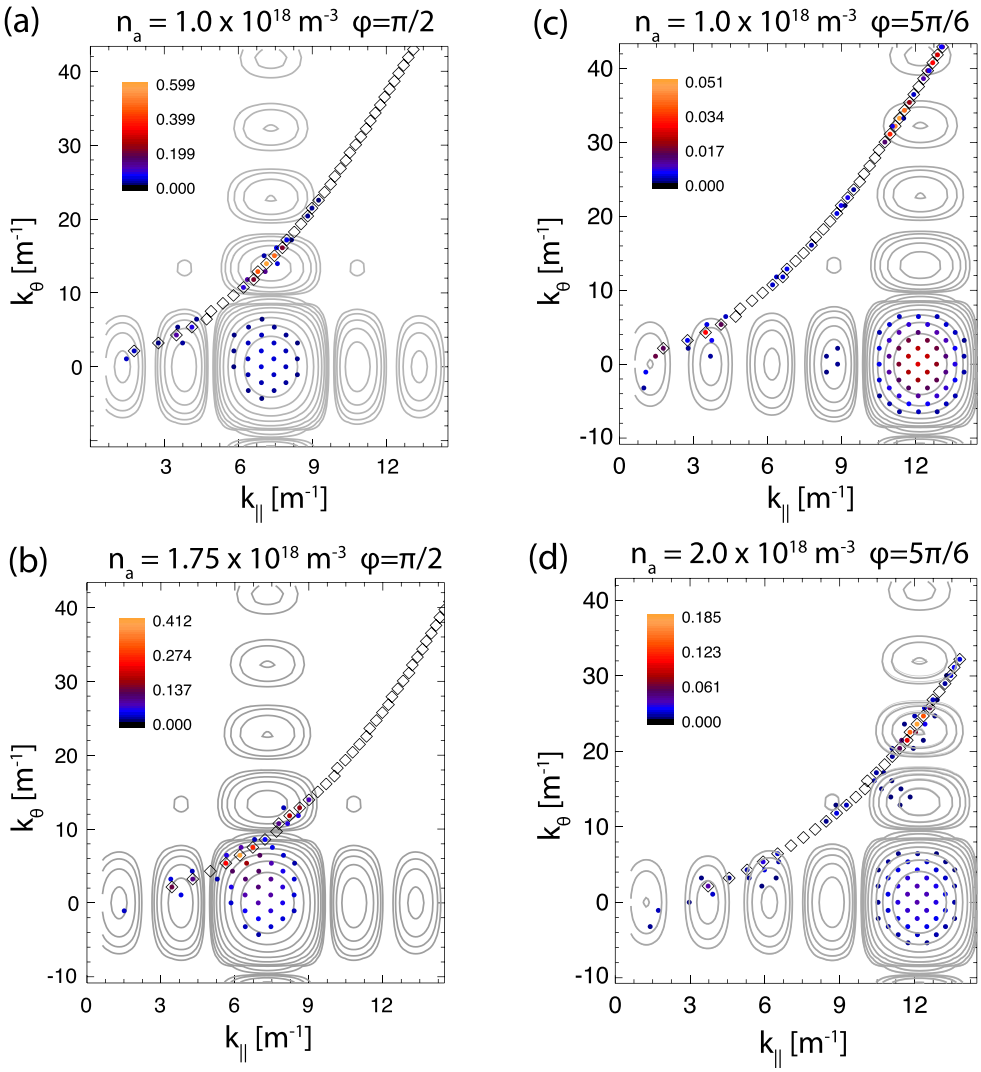

Figure 9. Location of the AR ridge (diamonds) and largest 50 ((*a*) and (*b*)) or 100 ((*c*) and (*d*)) modes (circles) relative to antenna spectral power (contour lines). (*a*) $\pi/2$ phasing and $n_a = 1.0 \times 10^{18}$ m^{-3}, (*b*) $\pi/2$ phasing and $n_a = 1.75 \times 10^{18}$ m^{-3}, (*c*) $5\pi/6$ phasing and $n_a = 1.0 \times 10^{18}$ m^{-3}, (*d*) $5\pi/6$ phasing and $n_a = 2.0 \times 10^{18}$ m^{-3}.

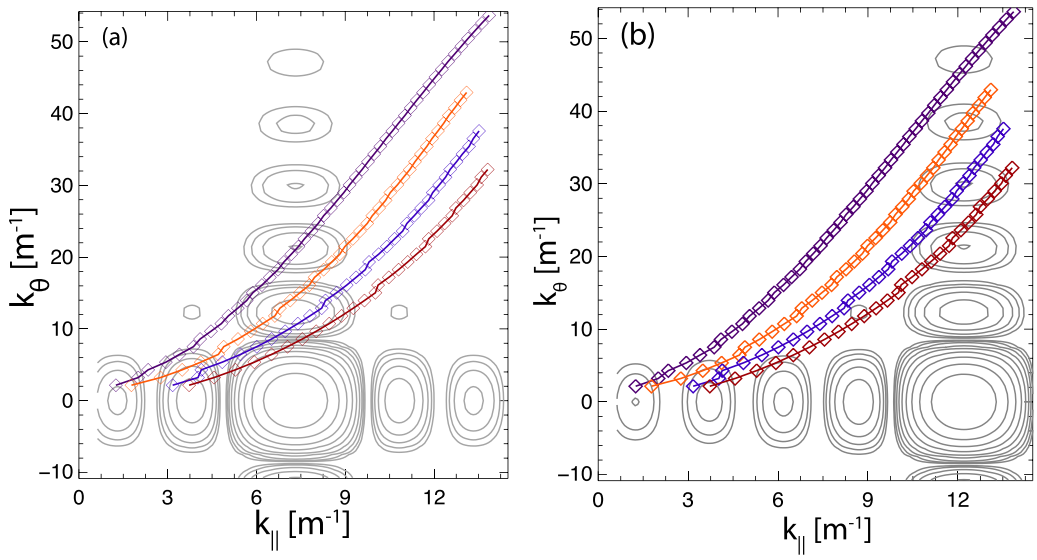

Figure 10. Contour plot of antenna spectral power and annulus resonances (diamonds) for different n_a: from upper left to lower right, $n_a = 0.5, 1.0, 1.5$, and 2.0×10^{18} m^{-3}. (*a*) $\pi/2$ inter-strap antenna phasing, and (*b*) $5\pi/6$. Increasing n_a shifts the AR ridge closer to the primary antenna spectral peaks.

Table 2. Effect of raising annulus density on both total loading and contribution from AR modes. Inter-strap phasing of $5\pi/6$.

Annulus Density	Loading				AR contribution		
	Total	Core (%)	Edge (%)	Oscillating	Core (%)	Edge (%)	Total (%)
0.5×10^{18}	0.79	0.62 (79%)	0.16 (19%)	0.03	3	97	23
1.0×10^{18}	1.12	0.77 (68%)	0.35 (32%)	0.07	8	97	36
1.5×10^{18}	1.63	1.05 (65%)	0.58 (35%)	0.20	14	94	43
2.0×10^{18}	2.16	1.46 (67%)	0.71 (33%)	0.39	18	91	42

antenna scales like m^{-2} (equation (4)), the percent AR contribution is not strong for $5\pi/6$ phasing. In fact, the wave power is more evenly distributed between modes; at $\pi/2$ phasing, 90% of the total power is carried by ~50 modes, whereas for $5\pi/6$ phasing it takes ~100 modes to reach 90%.

Finally, the 'slope' of the AR ridge at $k_{||} = 12.2$ m^{-1} is greater than that at $k_{||} = 7.3$ m^{-1}, so the AR ridge is likely to cross two adjacent azimuthal sidebands and is less likely to lie in a null between them as in figure 9(*b*) of the $\pi/2$ case. This explains why the edge loading increases monotonically with n_a for $5\pi/6$ phasing, in contrast to that in $\pi/2$ phasing. Also, for the same change in n_a, the m value of the strongest AR modes will drop more substantially for $5\pi/6$ phasing than for $\pi/2$ phasing.

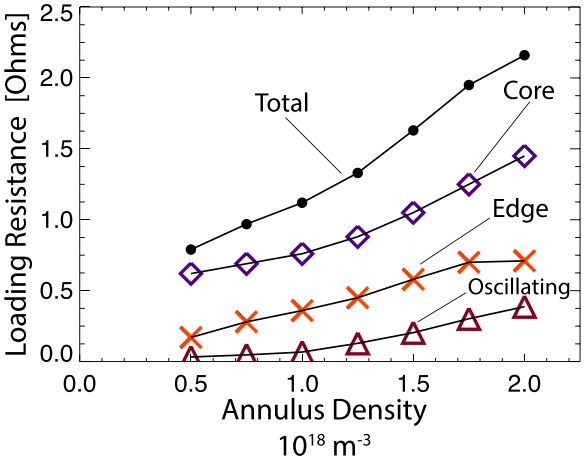

Figure 11. Trend in loading resistance as annulus density is increased: black circles, total loading; diamonds, core loading; crosses, edge loading; triangles, oscillating power.

5. Discussion

The previous sections present a conceptual framework in which the AR modes form a ridge on the $k_{||} - k_\theta$ plane, and where increasing the annulus density, for the current model parameters, moves this ridge closer to the peak in the antenna spectrum. For $\pi/2$ antenna phasing, the model predicts that the fraction of power trapped at the edge decreases as the annulus density is raised. This contradicts operational experience [6] and also results from full-wave calculations [14]. However, as the model does reproduce features of the experiments, such as over 50% of the wave power being trapped at the edge, it is important to see if varying certain model parameters changes the AR trajectory relative to the antenna peak. Potential parameters to vary include the core density and annulus width, which will be much greater for discharges with neutral beam injection.

We focus here on the potential role of the field tilt of NSTX. As a spherical torus, NSTX has a relatively weak toroidal field and a correspondingly large magnetic pitch at the outboard side, typically 30° to 40°. A preliminary approach to incorporating pitch is to rotate the projection of the mode k vectors on the $k_z - k_\theta$ plane. Figure 12 shows how a rotation of 30° can move the AR trajectory relative to the antenna spectral peak for $5\pi/6$ phasing, and the effect is quite dramatic compared to the unrotated case of figure 10(*b*). The rotated AR modes are decreased in k_θ, which greatly increases their amplitude since the azimuthal spectral weighting scales as m^{-2}. Also, since the AR trajectory is more horizontal (aligned with the k_z axis), we expect a broad range of AR modes to be excited by the axial sidebands of the antenna spectrum. While these

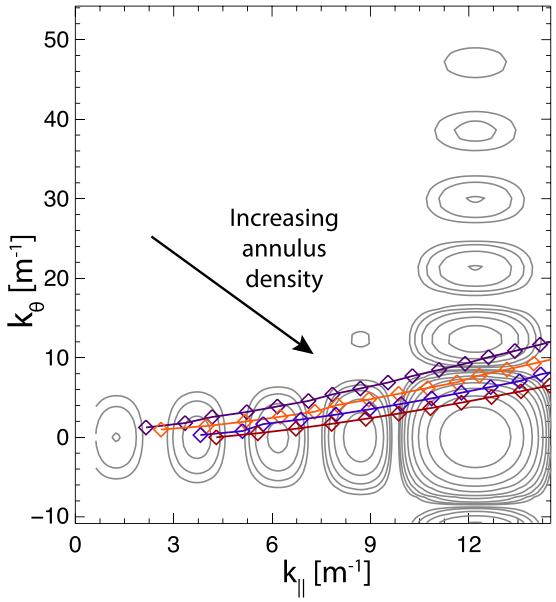

Figure 12. Effect of a 30° rotation on the position of the AR ridge relative to the antenna spectral peaks for different densities: 0.5×10^{18} m^{-3} (purple), 1.0×10^{18} m^{-3} (orange), 1.5×10^{18} m^{-3} (blue), 2.0×10^{18} m^{-3} (red).

speculations are based on a very coarse prescription of simply rotating k, they do suggest that field pitch could have a profound impact on the model and is worth studying in a more comprehensive treatment.

6. Conclusions

In a cylindrical magnetized cold-plasma model with a two-step density profile, there exists a special class of modes that fit a half wavelength in the combined annulus–vacuum region, have a high loading resistance, and propagate a large portion of their wave power at the edge. There is typically at most one such mode per azimuthal mode number m, and the $k_{\|}$ value of this mode increases with m. For the model parameters selected for this paper, the underlying reason for this relationship between $k_{\|}$ and m is that modes with the same value of $m+n$, with n denoting the number of radial nodes, maintain the half wavelength condition over a wide range of m. Viewed on the $k_{\|}-k_{\theta}$ plane, these modes lie on a trajectory whose distance from the antenna spectral peaks changes with parameters such as annulus density. We have computed the relative contributions of ARs and non-annulus-resonant modes as well as the fractional loading to the edge and core regions over a scan of the annulus density. As expected, edge loading is large when the AR modes contribute a substantial fraction to the total loading. We note cases where over half of the *total* wave power propagates at the edge with little flux of power between the edge and core. However, while the total loading always increases with annulus density, the edge loading behaves non-monotonically for the $\pi/2$-phasing case, as the AR ridge moves onto and off the azimuthal sideband of the antenna spectrum. In the case of $\pi/2$ phasing, this leads to the result where the fraction of power coupled to the core improves with the edge density, in contrast to the results of experiments and full-wave computations. The case of $5\pi/6$ phasing shows a degradation in core loading as the annulus density increases in the range of $0.5\text{–}1.0\times10^{18}$ m^{-3} but levels off in the range $1.0\text{–}2.0\times10^{18}$ m^{-3}. Magnetic pitch could play an important role; a coarse treatment indicates that rotating the k vectors of the modes by the magnetic-pitch angle at the antenna may bring the AR trajectory closer to the main spectral peak of the antenna, resulting in a large fraction of power being trapped at the edge.

Future work with this model will depend on initial results from HHFW experiments on NSTX-U. Improved diagnostic coverage will allow for more accurate quantification of the total power lost to the SOL and hopefully allow for definitive determination of the loss mechanism. Once this mechanism is identified, the proper absorption terms can be added to the model to compare the core and SOL damping rates and verify whether the annulus-resonant modes described here remain viable candidates for explaining SOL losses.

Acknowledgments

This work was supported by DOE Contract No. DE-AC02-09CH11466. This manuscript is based upon work supported by the U.S. Department of Energy, Office of Science, Office of Fusion Energy Sciences, and has been authored by Princeton University under Contract Number DE-AC02-09CH11466 with the U.S. Department of Energy. The publisher, by accepting the article for publication acknowledges, that the United States Government retains a non-exclusive, paid-up, irrevocable, world-wide license to publish or reproduce the published form of this manuscript, or allow others to do so, for United States Government purposes.

ORCID iDs

R.J. Perkins https://orcid.org/0000-0002-7216-0201

References

[1] Ren Y. *et al* 2015 Fast response of electron-scale turbulence to auxiliary heating cessation in National Spherical Torus Experiment *Phys. Plasmas* **22** 110701
[2] Fredrickson E., Taylor G., Bertelli N., Darrow D., Gorelenkov N., Kramer G., Liu D., Crocker N., Kubota S. and White R. 2015 Suppression of energetic particle driven instabilities with HHFW heating *Nucl. Fusion* **55** 013012
[3] Loarte A. *et al* 2015 Tungsten impurity transport experiments in Alcator C-Mod to address high priority research and development for ITER *Phys. Plasmas* **22** 056117
[4] Lerche E. *et al* and JET Contributors 2016 Optimization of ICRH for core impurity control in JET-ILW *Nucl. Fusion* **56** 036022
[5] Hosea J. *et al* 2007 HHFW heating efficiency on NSTX versus B_{ϕ} and antenna $k_{\|}$ *AIP Conf. Proc.* **933** 107–10
[6] Hosea J. *et al* and The NSTX Team 2008 High harmonic fast wave heating efficiency enhancement and current drive at longer wavelength on the National Spherical Torus Experimental *Phys. Plasmas* **15** 056104
[7] Ryan P.M., Ellis R., Hosea J.C., Kung C.C., LeBlanc B.P., Pinsker R.I., Taylor G. and Wilson J.R. 2011 Operating the Upgraded NSTX HHFW antenna array in an environment with Li-coated surfaces *AIP Conf. Proc.* 1406 101–4
[8] Hosea J.C. *et al* and The NSTX Team 2009 Recent fast wave coupling and heating studies on NSTX, with possible implications for ITER *AIP Conf. Proc.* 1187 105–12
[9] Perkins R.J. *et al* 2012 High-harmonic fast-wave power flow along magnetic field lines in the scrape-off layer of NSTX *Phys. Rev. Lett.* **109** 045001
[10] Stix T.H. 1992 *Waves in Plasmas* (Berlin: Springer)
[11] Perkins R.J. *et al* 2015 The contribution of radio-frequency rectification to field-aligned losses of high-harmonic fast wave power to the divertor in the National Spherical Torus eXperiment *Phys. Plasmas* **22** 042506
[12] Jaeger E.F. *et al* 2008 Simulation of high-power electromagnetic wave heating in the ITER burning plasma *Phys. Plasmas* **15** 072513
[13] Green D.L., Berry L.A., Chen G., Ryan P.M., Canik J.M. and Jaeger E.F. 2011 Predicting high harmonic ion cyclotron heating efficiency in tokamak plasmas *Phys. Rev. Lett.* **107** 145001
[14] Bertelli N. *et al* 2014 Full wave simulations of fast wave heating losses in the scrape-off layer of NSTX and NSTX-U *Nucl. Fusion* **54** 083004
[15] Taylor G. *et al* 2010 Advances in high-harmonic fast wave physics in the National Spherical Torus Experiment *Phys. Plasmas* **17** 056114
[16] Taylor G. *et al* 2012 High non-inductive fraction H-mode discharges generated by high-harmonic fast wave heating and current drive in the National Spherical Torus Experiment *Phys. Plasmas* **19** 042501
[17] Perkins R.J., Hosea J.C., Bertelli N., Taylor G. and Wilson J.R. 2016 Resonance in fast-wave amplitude in the periphery of

cylindrical plasmas and application to edge losses of wave heating power in tokamaks *Phys. Plasmas* **23** 070702
[18] D'Ippolito D. and Myra J. 2011 ICRF-edge and surface interactions *J. Nucl. Mater.* **415** S1001–4 (*Proc. of the 19th Int. Conf. on Plasma-Surface Interactions in Controlled Fusion*)
[19] LaBombard B., Boivin R.L., Greenwald M., Hughes J., Lipschultz B., Mossessian D., Pitcher C.S., Terry J.L., Zweben S.J. and Group A 2001 Particle transport in the scrape-off layer and its relationship to discharge density limit in Alcator C-Mod *Phys. Plasmas* **8** 2107–17
[20] Boedo J.A. *et al* and The NSTX Team 2014 Edge transport studies in the edge and scrape-off layer of the National Spherical Torus Experiment with Langmuir probes *Phys. Plasmas* **21** 042309
[21] Zweben S.J., Myra J.R., Davis W.M., D'Ippolito D.A., Gray T.K., Kaye S.M., LeBlanc B.P., Maqueda R.J., Russell D.A., Stotler D.P. and The NSTX-U Team 2016 Blob structure and motion in the edge of NSTX *Plasma Phys. Control. Fusion* **58** 044007
[22] Bertelli N. *et al* 2016 Full wave simulations of fast wave efficiency and power losses in the scrape-off layer of tokamak plasmas in mid/high harmonic and minority heating regimes *Nucl. Fusion* **56** 016019
[23] Allis W.P., Buchsbaum S.J. and Bers A. 1963 *Waves in Anisotropic Plasmas* vol 1 (Cambridge, MA: MIT Press)
[24] Bobkov V. *et al* 2016 Progress in reducing ICRF-specific impurity release in ASDEX upgrade and JET *Nucl. Mater. Energy* (https://doi.org/10.1016/j.nme.2016.10.026)
[25] Ramo S., Whinnery J.R. and Van Duzer T. 2008 *Fields and Waves in Communication Electronics* (New York: Wiley)
[26] Pècoul S., Heuraux S., Koch R. and Leclert G. 2002 Numerical modeling of the coupling of an ICRH antenna with a plasma with self-consistent antenna currents *Comput. Phys. Commun.* **146** 166–87
[27] Colas L., Heuraux S., Brémond S. and Bosia G. 2005 RF current distribution and topology of RF sheath potentials in front of ICRF antennae *Nucl. Fusion* **45** 767
[28] Ono M. 1995 High harmonic fast waves in high beta plasmas *Phys. Plasmas* **2** 4075–82
[29] Phillips C. *et al* and The NSTX Team 2009 Spectral effects on fast wave core heating and current drive *Nucl. Fusion* **49** 075015
[30] Lu L., Crombé K., Eester D.V., Colas L., Jacquot J. and Heuraux S. 2016 Ion cyclotron wave coupling in the magnetized plasma edge of tokamaks: impact of a finite, inhomogeneous density inside the antenna box *Plasms Phys. Control. Fusion* **58** 055001
[31] Hellsten T. and Laxåback M. 2005 Influence of coupling to spectra of weakly damped eigenmodes in the ion cyclotron range of frequencies on parasitic absorption in rectified radio frequency sheaths *Phys. Plasmas* **12** 032505
[32] Ryan P.M. *et al* and The NSTX Team 2003 High harmonic fast wave current drive experiments on NSTX *AIP Conf. Proc.* **694** 209–12